RIS-Enhanced Propagation and Exposure Evaluation in Modern Greenhouses

Felipe Oliveira Ribas*, Günter Vermeeren*, Thomas Zemen†, Milica Djordjevic†, Hamed Radpour†, Wout Joseph*
*WAVES, Ghent University/imec, 9052 Ghent, Belgium
†AIT Austrian Institute of Technology, 1210 Vienna, Austria

***Abstract*—Modern agriculture increasingly relies on high-capacity wireless links, motivating the use of millimeter-wave (mmWave) frequencies. However, in greenhouse environments, dense vegetation creates non-line-of-sight (NLoS) conditions that block mmWave signals and reduce reliability. Reconfigurable intelligent surfaces (RIS) can restore coverage by redirecting energy around obstacles, but their beamforming also changes the exposure environment. In this work, a realistic 3D greenhouse model is combined with Sionna ray-tracing at 26 GHz and FDTD dosimetry on a human model and a bumblebee, a widely used for insect pollination in commercial tomato cultivation. Results show that RIS restores blocked links with more than 40 dB SNR improvement, while human exposure remains well below ICNIRP 2020 limits and insect absorption increases by about four times. These findings highlight both the communication benefits and the altered exposure patterns associated with RIS deployment in smart horticulture.**

***Index Terms*—Propagation, exposure, agriculture, RIS.**

I. Introduction

Greenhouse agriculture increasingly relies on sensing and automation, which motivates robust, high-capacity wireless links. Millimeter-wave (mmWave) bands can offer the required throughput and latency for such applications [1], but their propagation is vulnerable to blockage and vegetation-induced scattering/polarization effects typical of greenhouses [2], [3].

Reconfigurable intelligent surfaces (RIS) are proposed to mitigate non-line-of-sight (NLoS) conditions by steering energy along favorable paths [4], [5]. While RIS can enhance coverage, it also redistributes electromagnetic fields within the environment, which raises questions about exposure for workers and for pollinators commonly used in greenhouses. Human exposure at mmWave frequencies is generally superficial and regulated by international guidelines, whereas insects can show frequency-dependent absorption linked to body dimensions [6], [7], [8].

This paper examines RIS-controlled propagation *and* exposure in a greenhouse scenario at 26 GHz. We employ a realistic 3D greenhouse model for site-specific ray tracing to obtain multipath propagation properties, then map those fields to finite-difference time-domain (FDTD) simulations for dosimetric on a human head phantom and on a bumblebee model. Our goal is to evaluate both propagation and exposure in RIS-assisted smart horticulture, linking connectivity performance with dosimetric outcomes.

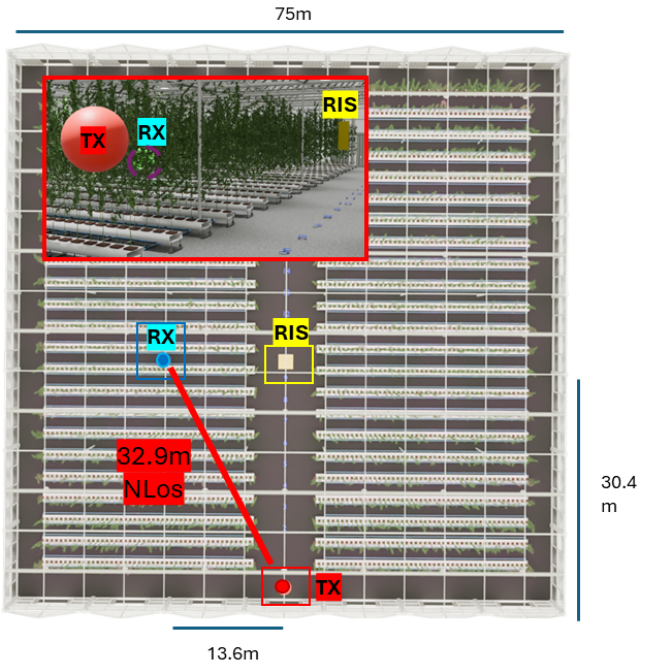

Fig. 1: Top view of greenhouse with device placement: TX at entrance, RX behind 10th row (NLoS, 32.9 m), and RIS in central corridor with LoS to TX. Inset: perspective view.

II. Methods

A. Scene and Geometry

A parametric greenhouse model is generated in Blender v4.5.1 (Stichting Blender Foundation, Amsterdam) and exported to Sionna via the Mitsuba add-on [9]. The geometry is based on typical industrial greenhouse layouts and dimensions [10], with an overall size of $75 \times 75 \times 10$ m. Plants are distributed along 20 rows of crop beds to reproduce the growth pattern of greenhouse tomatoes, which are commonly cultivated with vertical support wires guiding the main stem upward and enabling tall canopies [11]. Randomized rotation and size were applied to individual plants to ensure variability and avoid artificial corridors.

Electromagnetic properties of glass, concrete, and metal are taken from the ITU-R P.2040-3 database [12] as implemented in the Sionna [13] materials library, while vegetation parameters were assigned from literature values reported for 20–30 GHz [14]. The resulting geometry captures realistic blockage and foliage scattering while remaining computationally feasible.

978-88-31299-12-1/26/$31.00 ©2026 IEEE

B. Ray Tracing and Link-Level Evaluation

Propagation is simulated using Sionna v0.19.2 [13] at 26 GHz with a 200 MHz bandwidth.

The TX is mounted near the ceiling at the greenhouse entrance, approximately 5 m above the ground. The RX is positioned behind the 10th vegetation row at a height of about 2 m and more than 30 m away from the TX, without direct line-of-sight. A RIS panel is installed in the main corridor at a comparable height to the TX, maintaining line-of-sight (LoS) to it and oriented toward the RX, as summarized in Table I.

The TX employed a 4×4 TR 38.901 planar array (V-pol) with directional beamforming toward the RIS, while the RX was a single-element antenna (V-pol). The RIS was a 100×100 dense grid of elements with $\lambda/2$ spacing (corresponding to an aperture of approximately 0.58×0.58 m at 26 GHz). It operated in *phase-gradient reflector* mode, with its phase profile optimized to redirect the incoming energy from the TX toward the RX.

Two scenarios were evaluated for comparison: a *no-RIS* case including only natural multipath components (reflection, diffraction, and scattering), and a *RIS-assisted* case including these plus the RIS-assisted path. The link budget was obtained from the coherent sum of all received paths, accounting for antenna gains and RIS-assisted reflections. The corresponding received power P_{rx} was then used to calculate the signal-to-noise ratio (SNR) relative to the thermal noise floor, with $N_0 = kTB$ ($T = 290$ K, $B = 200$ MHz).

This configuration was deliberately chosen to create a challenging non-line-of-sight (NLoS) link behind dense vegetation, where natural multipath is weak and unstable. Placing the RX behind the 10th row ensured strong attenuation, while positioning the RIS in the main corridor with LoS to both TX and RX provided a plausible deployment site within a greenhouse. The use of a large-scale 100×100-element RIS was intended to clearly expose the RIS-assisted path and to establish a workflow for identifying and quantifying engineered multipath in comparison to natural scattering.

The angular distribution of incoming paths at the RX was also recorded, allowing us to quantify the spread of arrival angles. This captures the variability of normal multipath compared to the highly directional RIS-assisted path, which is relevant for both interference and exposure analysis.

C. FDTD Dosimetry

Multipath components from Sionna (Fig. 2A) were imported into Sim4Life v9.0 (ZMT Zurich MedTech, Switzerland) as coherent plane waves, with direction, amplitude, and phase [15] preserved and amplitudes scaled from path gains using free-space impedance. Because per-path polarization was not available, all paths were assigned vertical polarization at the RX plane for consistency. Two phantoms were evaluated. For humans, the *Duke* adult male model from the IT'IS Virtual Family [16] was used. Only the head was simulated, since at 26 GHz penetration depth is below 1 mm and exposure is confined to superficial tissues [17]. Electromagnetic properties were assigned from the IT'IS database [18].

TABLE I: Configuration of devices in the Sionna greenhouse simulation

Parameter	**Value**
Carrier frequency	26 GHz, 200 MHz bandwidth
Transmitter (TX)	Planar array, 4×4 elements, 0.25λ spacing, V polarization
Receiver (RX)	Single-element dipole antenna, V polarization
TX coordinates	(0, -35, 5) m
RX coordinates	(-17, -5, 2) m
Transmit power P_{tx}	24 dBm
RIS coordinates	(4, -5, 5) m
RIS configuration	100×100 element grid
TX–RX distance	≈ 32.9 m
TX–RIS distance	≈ 30.4 m
RIS–RX distance	≈ 13.6 m
TX–RIS–RX path length	≈ 44.0 m

For insects, a 15 mm worker bumblebee (*Bombus terrestris*) was reconstructed from a Sketchfab [19] photogrammetry model, rescaled for anatomical accuracy, and modeled as a homogeneous phantom with dielectric parameters representative of the exoskeleton reported in [20] ($\varepsilon_r = 14.3$, $\sigma = 18.8$ S/m). Cubic source regions of $300\times300\times300$ mm^3 and $40\times40\times40$ mm^3 were defined around the human head and insect models, respectively (Fig. 2B,C). In all cases, the phantoms were centered within their respective cubic source regions at the RX coordinates, reflecting realistic RIS-assisted propagation conditions. Grid resolution was set to 1.0 mm for the human head and 0.05 mm for the bumblebee, reflecting anatomical scale and computational feasibility.

Each phantom was simulated at four orientations relative to the RIS (0°, 90°, 180°, 270°). To assess the impact of propagation components, two configurations were considered: a *no-RIS* case including only normal multipath (reflection, diffraction, scattering), and a *RIS* case including these plus the RIS-assisted component.

Exposure metrics differed for the human and insect. For humans, only the head was simulated, since at 26 GHz penetration depth is below 1 mm [17]. We evaluated the localized head-averaged specific absorption rate (SAR), the peak spatially averaged surface power density S_{ab} over a 4 cm^2 area in line with ICNIRP guidelines [17], and the absorbed power P_{abs} (W). For insects, we used the total absorbed power P_{abs} and whole-body SAR.

III. Results and Discussion

A. Propagation

In the baseline (no RIS) greenhouse scenario, no line-of-sight (LoS) path was observed due to dense vegetation blocking the direct signal. Multipath was dominated by foliage-induced scattering (134 paths, strongest –75.6 dB), while diffraction was marginal (12 paths, –103.6 dB) and reflection negligible (7 paths, –117.2 dB). As a result, the coherent SNR at the RX was only 2.3 dB over 200 MHz—insufficient for reliable connectivity.

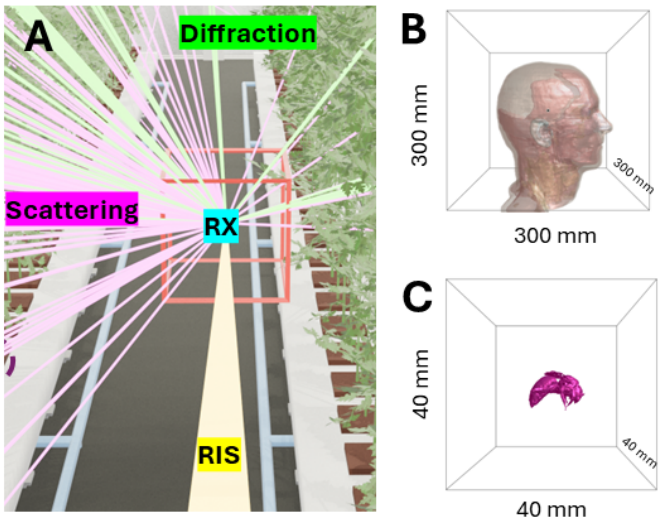

Fig. 2: FDTD setup. (A) RX position with incoming paths and example cubic source region. (B) Human head phantom (*Duke*) in the $300 \times 300 \times 300\,\mathrm{mm}^3$ region. (C) Bumblebee model in the $40 \times 40 \times 40\,\mathrm{mm}^3$ region.

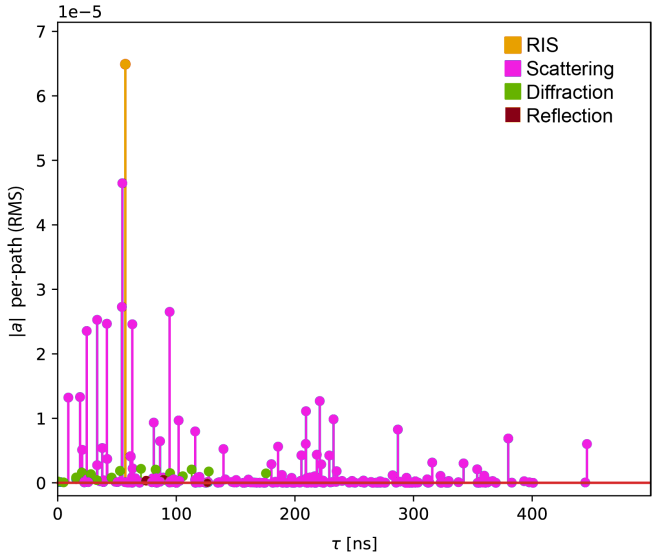

Fig. 3: Channel impulse response showing the per-path RMS amplitude $|a|$ as a function of delay τ. The RIS-assisted path (yellow) arrives slightly later than the earliest multipath components due to its longer TX–RIS–RX distance, but dominates with the highest amplitude. Scattering contributions (purple) are numerous but weaker, while diffraction (green) and reflection (red) are negligible.

When the RIS is activated, a new strong controllable path appears, dominating over all natural multipath contributions, as shown in the channel impulse response of Fig. 3

Analysis of arrival directions confirmed this picture. Natural multipath components arrived over a very wide azimuth spread ($\sigma_{\mathrm{Az}} \approx 90°$) for both scattering and diffraction, with reflections similarly weak and diffuse (Fig. 2A). In contrast, the RIS-assisted path was narrowly concentrated ($\sigma_{\mathrm{Az}} \approx 15°$), providing a deterministic, high-gain beam that minimized destructive interference at the RX.

Employing a large-scale 100×100-element RIS, this provided

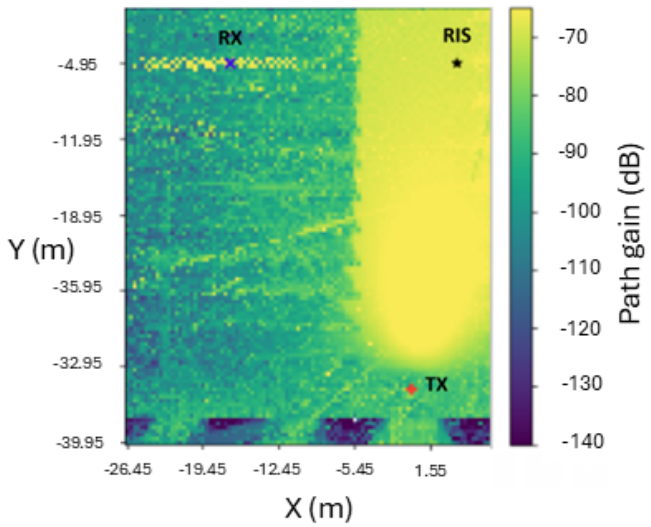

Fig. 4: Coverage map of path gain (dB) at 2 m height with 0.1 m cell resolution, including all multipath components. A strong RIS-assisted path is visible along the row at $Y = -4.95\,\mathrm{m}$.

a coherent gain of 43.5 dB relative to the baseline, boosting the SNR to 45.8 dB and restoring a robust link (Fig. 4).

These propagation trends are consistent with prior studies of radio transmission through vegetation, where scattering often dominates in NLoS conditions at high frequencies. Vegetation is known to cause strong attenuation and diffuse scattering of mmWave signals, making direct reflection paths weak or absent [21], [3], [14].

In greenhouse-like environments with extensive glass surfaces and minimal supporting structure, reflection contributions tend to be low due to glass's modest reflectivity at mmWave frequencies [22]. The metal support beams might produce occasional diffraction or localized scattering, but their effect is small compared to foliage-induced scattering.

Overall, the propagation environment is governed by foliage scattering, which is both weak and highly variable with wind, moisture, and seasonal morphology [23]. In contrast, RIS panels provide a far more stable [24] and controllable alternative for shaping the propagation environment. For greenhouse monitoring and automation, where stable connectivity is critical, the deterministic RIS path provides robustness unavailable from foliage scattering alone.

1) Human head: At 26 GHz, the RIS case increases the absorbed power and surface-averaged density compared to the no-RIS baseline, but all values remain far below ICNIRP limits ($10\,\mathrm{W/m}^2$, 0.08 W/kg whole-body) [17]. No substantive differences are observed between head orientations.

Specifically, the absorbed power rises from $3.83 \times 10^{-6}\,\mathrm{W}$ without RIS to $9.92 \times 10^{-6}\,\mathrm{W}$ with RIS, while the surface-averaged density $S_{\mathrm{ab}}(4\,\mathrm{cm}^2)$ increases from 5.94×10^{-4} to $1.39 \times 10^{-3}\,\mathrm{W/m}^2$. The localized head-averaged SAR similarly remains negligible, increasing from 5.47×10^{-8} to $1.42 \times 10^{-7}\,\mathrm{W/kg}$. All these values are more than $10^5\times$ below ICNIRP limits.

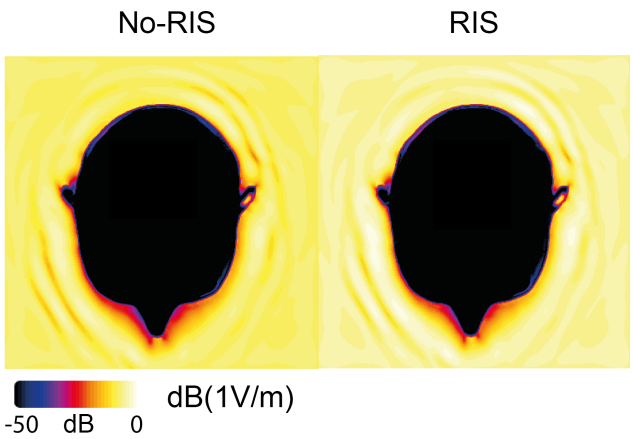

Fig. 5: $|\mathbf{E}|$ on a head XY slice at 26 GHz. No-RIS (left) vs. RIS (right); identical setup and color scale (–50 to 0 dB re 1 V/m).

These findings align with prior RIS-assisted studies: RIS boosts local fields, yet human exposure remains within safety limits [25], [26]. At 26 GHz, absorption is skin-limited (penetration depth below 1 mm) [17], hence ICNIRP (2020) uses the 4 cm^2 peak surface power density above 6 GHz [17]. As shown in Fig. 5, fields are surface-confined in both no-RIS and RIS cases; the RIS mainly increases surface magnitude, not depth.

2) Insect: For the bumblebee model, the RIS amplified absorption by approximately 2.5–4× compared to natural multipath. Total absorbed power increased from $(1.07\text{–}1.72)\times10^{-2}$ W in the no-RIS case to $(2.28\text{–}6.29)\times10^{-2}$ W with RIS, while the whole-body SAR rose from $(1.54\text{–}1.58)\times10^{-4}$ to $(3.86\text{–}4.00)\times10^{-4}$ W/kg.

Orientation played a clear role: when the bumblebee faced the RIS, the absorbed power reached 6.29×10^{-2} W with a whole-body SAR of 4.00×10^{-4} W/kg, compared to only 2.28×10^{-2} W and 3.86×10^{-4} W/kg when the insect was oriented away from it. This occurs because elongated bodies couple more efficiently when their long axis is aligned with the incident electric field [8], [27].

Figure 6 illustrates how the RIS concentrates fields, creating localized high-intensity regions (bright yellow areas in panels 2A–2B) that are absent in normal multipath propagation. Unlike humans, insects are not covered by exposure guidelines [28].

Our findings suggest that RIS panels, while beneficial for connectivity, may create local exposure hotspots [29] that insects encounter repeatedly during foraging flights. Such altered exposure patterns could influence flight behavior or pollination efficiency [30], potentially resulting in economic losses linked to reduced pollination services [31]. These aspects warrant further investigation.

IV. Conclusion

This work combined realistic greenhouse modeling with ray tracing and FDTD simulations to evaluate RIS-assisted mmWave links. We show that RIS restores connectivity in blocked links and improves received power by over 40 dB. At the same time, RIS alters the exposure environment: human

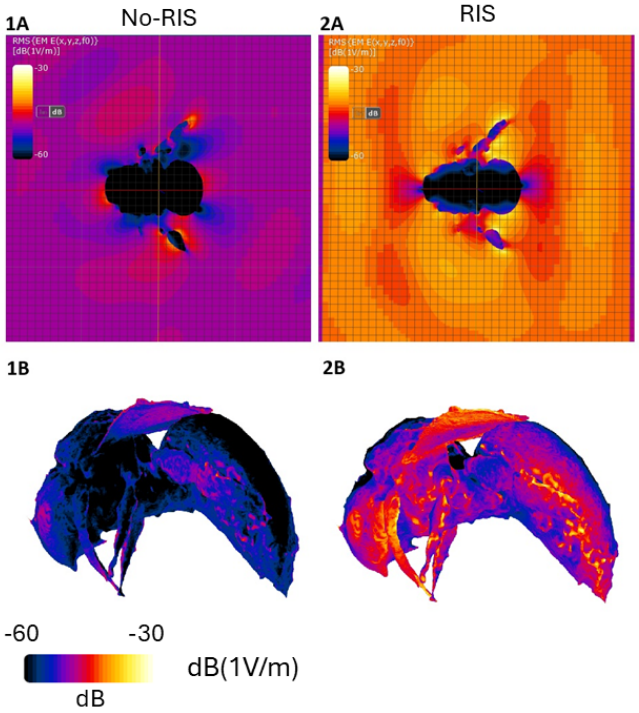

Fig. 6: Electric field distribution at 26 GHz for the bumblebee model. (1A) Field slice for the no-RIS path. (2A) Field slice for the RIS-assisted path. (1B) Surface field distribution for the no-RIS path. (2B) Surface field distribution for the RIS-assisted path. All plots use the same color scale (-60 to -30 dBV/m, reference 1 V/m). Model reference [19]

exposure remains far below international safety limits, while insect absorption increases by about four times depending on orientation. These results illustrate a trade-off—RIS enhances smart farming connectivity but may also influence pollinator exposure—highlighting the need to assess both communication performance and ecological impacts when deploying RIS in greenhouses.

Future work will investigate exposure across different RIS deployments to better quantify potential ecological effects.

References

[1] R. Ford, M. Zhang, M. Mezzavilla, S. Dutta, S. Rangan, and M. Zorzi, "Achieving ultra-low latency in 5g millimeter wave cellular networks," *IEEE Communications Magazine*, vol. 55, no. 3, pp. 196–203, 2017.

[2] R. F. Caldeirinha, *Radio characterisation of single trees at micro- and millimetre wave frequencies*. University of South Wales (United Kingdom), 2001.

[3] D. Cama-Pinto, M. Damas, J. A. Holgado-Terriza, F. M. Arrabal-Campos, F. Gómez-Mula, J. A. Martínez-Lao, and A. Cama-Pinto, "Empirical model of radio wave propagation in the presence of vegetation inside greenhouses using regularized regressions," *Sensors*, vol. 20, no. 22, p. 6621, 2020.

[4] W. Khawaja, O. Ozdemir, Y. Yapici, F. Erden, and I. Guvenc, "Coverage enhancement for nlos mmwave links using passive reflectors," *IEEE Open Journal of the communications Society*, vol. 1, pp. 263–281, 2020.

[5] J. Rains, A. Tukmanov, T. J. Cui, L. Zhang, Q. H. Abbasi, M. A. Imran, *et al.*, "High-resolution programmable scattering for wireless coverage enhancement: An indoor field trial campaign," *IEEE Transactions on Antennas and Propagation*, vol. 71, no. 1, pp. 518–530, 2022.

[6] A. Hirata, Y. Diao, T. Onishi, K. Sasaki, S. Ahn, D. Colombi, V. De Santis, I. Laakso, L. Giaccone, W. Joseph, *et al.*, "Assessment of human exposure to electromagnetic fields: Review and future directions," *IEEE*

Transactions on Electromagnetic Compatibility, vol. 63, no. 5, pp. 1619–1630, 2021.

[7] L. Hardell, M. Nilsson, T. Koppel, and M. Carlberg, "Aspects on the international commission on non-ionizing radiation protection (icnirp) 2020 guidelines on radiofrequency radiation," *J Cancer Sci Clin Ther*, vol. 5, no. 2, pp. 250–85, 2021.

[8] A. Thielens, D. Bell, D. B. Mortimore, M. K. Greco, L. Martens, and W. Joseph, "Exposure of insects to radio-frequency electromagnetic fields from 2 to 120 ghz," *Scientific reports*, vol. 8, no. 1, p. 3924, 2018.

[9] mitsuba renderer, "Mitsuba blender add-on." https://github.com/mitsuba-renderer/mitsuba-blender. Accessed: 2025-10-01.

[10] B. Von Elsner, D. Briassoulis, D. Waaijenberg, A. Mistriotis, C. Von Zabeltitz, J. Gratraud, G. Russo, and R. Suay-Cortes, "Review of structural and functional characteristics of greenhouses in european union countries, part ii: Typical designs," *Journal of agricultural engineering research*, vol. 75, no. 2, pp. 111–126, 2000.

[11] M. Kreuger, L. Meeuws, and G. Meeuws, "Applications for breeding and high-wire tomato production in plant factory," in *Smart Plant Factory: The Next Generation Indoor Vertical Farms*, pp. 289–299, Springer, 2018.

[12] P. Series, "Effects of building materials and structures on radiowave propagation above about 100 mhz," *recommendation itu-r*, pp. 2040–1, 2015.

[13] F. A. Aoudia, J. Hoydis, M. Nimier-David, S. Cammerer, and A. Keller, "Sionna rt: Technical report," *arXiv preprint arXiv:2504.21719*, 2025.

[14] J. Blumenstein, R. Zavorka, J. Vychodil, T. Mikulasek, J. Wojtun, J. M. Kelner, C. Ziolkowski, R. Shukla, M. Hofer, T. Zemen, *et al.*, "Stochastic 3d foliage modeling at 80 ghz: Experimental validation and ray tracing simulations," *IEEE Antennas and Wireless Propagation Letters*, 2025.

[15] S. Shikhantsov, A. Thielens, G. Vermeeren, P. Demeester, L. Martens, and W. Joseph, "Numerical assessment of human emf exposure to collocated and distributed massive mimo deployments in an industrial indoor environment," *IEEE Transactions on Electromagnetic Compatibility*, vol. 65, no. 4, pp. 960–971, 2023.

[16] A. Christ, W. Kainz, E. G. Hahn, K. Honegger, M. Zefferer, E. Neufeld, W. Rascher, R. Janka, W. Bautz, J. Chen, *et al.*, "The virtual family—development of surface-based anatomical models of two adults and two children for dosimetric simulations," *Physics in Medicine & Biology*, vol. 55, no. 2, p. N23, 2009.

[17] I. C. on Non-Ionizing Radiation Protection *et al.*, "Guidelines for limiting exposure to electromagnetic fields (100 khz to 300 ghz)," *Health physics*, vol. 118, no. 5, pp. 483–524, 2020.

[18] C. Baumgartner, P. A. Hasgall, F. Di Gennaro, E. Neufeld, B. Lloyd, M. C. Gosselin, D. Payne, A. Klingenböck, and N. Kuster, "IT'IS Database for Thermal and Electromagnetic Parameters of Biological Tissues, Version 5.0." IT'IS Foundation, Virtual Population Project, 2025. Accessed: 21 August 2025.

[19] Yuichi Kano, "Cc0 bumblebee." https://sketchfab.com/3d-models/cc0-bumblebee-f0aac424f44b48cf9217ffe126ace5ca, 2020. 3D model obtained via photogrammetry. Licensed under CC0 Public Domain.

[20] V. Jeladze, G. Korkotadze, A. Thielens, B. Partsvania, T. Nozadze, and R. Zaridze, "Estimation of the specific absorption rate for a honey bee exposed to radiofrequency electromagnetic fields from 2.5 to 100 ghz," in *2023 IEEE XXVIIIth International Seminar/Workshop on Direct and Inverse Problems of Electromagnetic and Acoustic Wave Theory (DIPED)*, pp. 180–185, 2023.

[21] N. Savage, D. Ndzi, A. Seville, E. Vilar, and J. Austin, "Radio wave propagation through vegetation: Factors influencing signal attenuation," *Radio Science*, vol. 38, no. 5, pp. 9–1, 2003.

[22] S. Y. Jun, D. Caudill, J. Chuang, P. B. Papazian, A. Bodi, C. Gentile, J. Senic, and N. Golmie, "Penetration loss at 60 ghz for indoor-to-indoor and outdoor-to-indoor mobile scenarios," in *2020 14th European Conference on Antennas and Propagation (EuCAP)*, pp. 1–5, IEEE, 2020.

[23] J. Bataineh, *Electromagnetic scattering through trees and vegetation at microwave and millimetre-wave frequencies*. PhD thesis, University of Bath, 2022.

[24] J. B. Gros, G. Lerosey, F. Lemoult, M. Lodro, S. Greedy, and G. Gradoni, "Multi-path fading and interference mitigation with reconfigurable intelligent surfaces," *arXiv preprint arXiv:2206.08290*, 2022.

[25] M. S. Elbasheir, R. A. Saeed, and S. Edam, "Measurement and simulation-based exposure assessment at a far-field for a multitechnology cellular site up to 5g nr," *IEEE Access*, vol. 10, pp. 56888–56900, 2022.

[26] S. Gallucci, M. Benini, S. Fiocchi, G. Tognola, and M. Parazzini, "6g ris in indoor environments: Assessment of exposure variability in human users and non-users," *IEEE Open Journal of Antennas and Propagation*, 2025.

[27] E. De Borre, W. Joseph, R. Aminzadeh, P. Müller, M. N. Boone, I. Josipovic, S. Hashemizadeh, N. Kuster, S. Kühn, and A. Thielens, "Radio-frequency exposure of the yellow fever mosquito (a. aegypti) from 2 to 240 ghz," *PLOS computational biology*, vol. 17, no. 10, p. e1009460, 2021.

[28] B. B. Levitt, H. C. Lai, and A. M. Manville, "Effects of non-ionizing electromagnetic fields on flora and fauna, part 2 impacts: how species interact with natural and man-made emf," *Reviews on Environmental Health*, vol. 37, no. 3, pp. 327–406, 2022.

[29] Z. Cui, F. Minucci, R. Hersyandika, R. M. Alonso, A. P. Guevara, H. Sallouha, and S. Pollin, "Electric field evaluation of reconfigurable intelligent surface in wireless networks," in *2024 IEEE International Symposium on Dynamic Spectrum Access Networks (DySPAN)*, pp. 420–428, IEEE, 2024.

[30] S. Shepherd, M. Lima, E. Oliveira, S. Sharkh, C. Jackson, and P. Newland, "Extremely low frequency electromagnetic fields impair the cognitive and motor abilities of honey bees," *Scientific reports*, vol. 8, no. 1, pp. 1–9, 2018.

[31] C. Lippert, A. Feuerbacher, and M. Narjes, "Revisiting the economic valuation of agricultural losses due to large-scale changes in pollinator populations," *Ecological Economics*, vol. 180, p. 106860, 2021.